PHYSICAL REVIEW B **108**, 104108 (2023)

Pressure-dependent distortions in quasi-two-dimensional magnetic CrOCl at low temperatures

Achim M. Schaller,[1] Maxim Bykov,[2] Elena Bykova,[2,*] Konstantin Glazyrin,[3]
Toms Rekis,[1] and Sander van Smaalen[1,†]
[1]*Laboratory of Crystallography, University of Bayreuth, 95440 Bayreuth, Germany*
[2]*The Earth and Planets Laboratory, Carnegie Institution for Science, Washington, District of Columbia 20015, USA*
[3]*Deutsches Elektronen-Synchrotron DESY, Notkestr. 85, 22607 Hamburg, Germany*

(Received 25 March 2023; accepted 11 September 2023; published 22 September 2023)

The layered van der Waals compound CrOCl is frustrated for antiferromagnetic (AFM) order, because of its orthorhombic *Pmmn* symmetry that supports a triangular lattice of magnetic Cr^{3+} ions. At ambient pressure, CrOCl develops incommensurate AFM order below $T_c = 27.2$ K, and it becomes AFM ordered with a fourfold magnetic supercell below the Néel temperature $T_{N,1\mathrm{bar}} = 13.5$ K. This AFM order is facilitated by an **a**-unique monoclinic lattice distortion. At room temperature, CrOCl remains orthorhombic up to at least 57 GPa. It develops a structural modulation that is the result of the optimization of the packing of Cl atoms within the van der Waals gap. Single-crystal x-ray diffraction (SXRD) at conditions of high pressure and low temperature (HPLT) uncover three novel HPLT phases of CrOCl. Instead of an **a**-unique monoclinic lattice, major distortions are found for the lattice parameter angles β and γ, resulting in a **c**-unique HPLT phase at 35 K, a triclinic HPLT phase at both 14 and 35 K, and a structurally modulated, triclinic phase at yet higher pressures. The structurally modulated phases appear at nearly the same critical pressures of $15.0 < p_c < 16.0$ GPa, and they are of a similar nature at 14, 35, and 293 K, despite the different lattice symmetries. The unmodulated triclinic phase is proposed to lead to more favorable distortions within the double layers CrO than is possible within the high-symmetry structures at equivalent (p, T) conditions. Incommensurate magnetic order or commensurate AFM order may appear with the **c**-unique HPLT phase at 35 K. This then implies a substantial pressure dependence of the magnetic transitions of $\Delta T_c/\Delta p = 1.42$ K/GPa or $\Delta T_N/\Delta p = 4.1$ K/GPa, respectively. The present finding of substantial lattice distortions involving the angle γ may have ramifications for monolayer structures of CrOCl.

DOI: 10.1103/PhysRevB.108.104108

I. INTRODUCTION

Van der Waals layered low-dimensional magnetic materials have gained considerable interest over the past years, as they have the potential to be used for novel spintronic applications and to provide magnetic properties that are susceptible to various external stimuli [1–4]. Among those materials, CrOCl has an antiferromagnetically (AFM) ordered state below $T_{N,1\mathrm{bar}} = 13.5$–$14.0$ K [5–8], which persists in mechanically exfoliated few-layer-thick flakes [9] and monolayers [10]. This robust AFM order can be explained by strong intralayer interactions, while the interlayer coupling across the van der Waals gap is weak (Fig. 1) [9,10]. CrOCl has a sizable magnetoelastic coupling [5,6,9,12]. This opens up the possibility of controlling the magnetic coupling and the magnetic state by manipulating structural parameters via mechanical strain [13–17]. Hydrostatic pressure is a viable tool to do so [18–22]. Since CrOCl is a quasi-two-dimensional (2D) magnetic compound due to its weak interlayer coupling [9], pressurizing the bulk material at low temperatures yields also relevant insights for CrOCl in the few-to-single layer range.

The nuclear and magnetic phase diagram of CrOCl has been studied in dependence on temperature at 1 bar [5,6,8,9,12,23,24] and as a function of pressure at 293 K [25]. At ambient conditions CrOCl is paramagnetic with orthorhombic *Pmmn* symmetry [23,26,27]. Upon cooling, an incommensurately modulated magnetic phase develops below $T_{c2} = 27.5$ K [5–7,9]. It is followed by a transition at the Néel temperature $T_N = 13.5$ K towards a commensurately modulated magnetic phase [5–7]. Magnetic order follows an unconventional spin density wave (SDW) propagating along **b** [7]. The characteristic mechanism at T_N is an orthorhombic-to-monoclinic lattice distortion towards an **a**-unique monoclinic phase, which lifts the geometric frustration of antiferromagnetic order on the orthorhombic lattice [5]. Of the three possible monoclinic symmetries, the **a**-unique monoclinic lattice distortion has the largest effect on lifting the degeneracy for AFM order in CrOCl [5].

The application of hydrostatic pressure to CrOCl at room temperature triggers a different mechanism. Initially, the van der Waals gap shrinks in a simple manner. A normal-to-incommensurate phase transition proceeds at $p_c \approx 16$ GPa for all *M*OCl (*M* = Ti, V, Cr, Fe) [25]. This structural transition is independent from changes in the electronic or magnetic structures of *M*OCl [25]. Instead, it is governed by an optimization of the interlayer packing of chlorine atoms through displacive modulations of the Cl atoms along **a** and **c**, which avoids unfavorably short Cl $\cdots$ Cl contacts [25].

---

[*] Present address: Mineralogie/Kristallographie, Institut für Geowissenschaften, Goethe-Universität Frankfurt, 60438 Frankfurt am Main, Germany.

[†] smash@uni-bayreuth.de

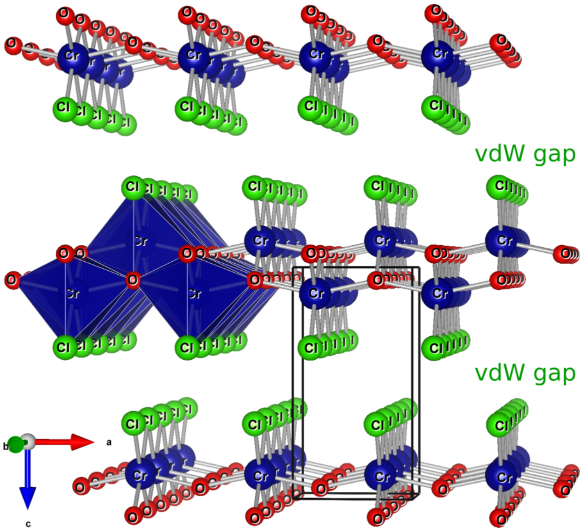

FIG. 1. Perspective view of the crystal structure of CrOCl at ambient conditions (space group *Pmmn*), highlighting the van der Waals (vdW) gap between the layers of the structure. Each Cr^{3+} ion is surrounded by two chlorine and four oxygen atoms in a distorted octahedral coordination, as indicated by (blue) polyhedra, thus forming CrOCl bilayers. The Cr^{3+} ions form chains with short Cr–Cr distances, which run along the **b**-axis. The unit cell is indicated by solid black lines. Drawn with VESTA [11].

Here, we combine high-pressures (HP) with low temperatures (LT), in order to investigate by single-crystal x-ray diffraction (SXRD) the structural pressure response of the magnetically ordered phases of CrOCl. We report the results of HPLT SXRD at temperatures of 14 and 35 K, with pressures up to 46.7 GPa. We characterize in detail the different types of lattice and structural distortions, which include three new monoclinic and triclinic phases in CrOCl. Furthermore, we discuss the effect of pressure-induced structural changes on the magnetic order and Néel temperature. In order to gain an understanding of *M*OCl in general, we compare the pressure- and temperature-dependent evolution with that of FeOCl [22]. As CrOCl is a quasi-2D magnetic material, the information on the (p, T) phase diagram will provide not only valuable information for further experimental and theoretical studies on bulk material, but also for the understanding of the properties of few-layer CrOCl.

II. EXPERIMENT

A. Sample preparation

CrOCl crystals were grown by chemical vapor transport in evacuated quartz-glass ampoules according to procedures described in [26,28], employing stoichiometric amounts of $CrCl_3$ (Alfa Aesar, 99.9%) and Cr_2O_3 (Alfa Aesar, 99.997%). $HgCl_2$ (Acros, $> 99.5\%$) was used as transport agent. Crystals grow as thin flakes with the large facets perpendicular to the reciprocal basis vector $\mathbf{c}^*$. They were cut-to-size for the experiments with diamond anvil cells (DACs).

HPLT experiments were performed with aid of DACs containing Boehler-Almax type anvils [29] with culet diameters of 300 μm and Rhenium gaskets. Two DACs were loaded with single crystals of CrOCl and neon as quasi-hydrostatic pressure-transmitting medium (PTM) [30].

B. Single-crystal x-ray diffraction and data processing

Two independent HPLT SXRD experiments were conducted *in situ* at beamline P02.2 of PETRA III in Hamburg, Germany. Experiment 1 employed radiation of wavelength $\lambda = 0.2889$ Å. It was performed at a temperature of 35 K on DAC-1 containing a single crystal of area 49×24 μm^2. Experiment 2 employed radiation of wavelength $\lambda = 0.2897$ Å. It was performed at a temperature of 14 K on DAC-2 containing a single crystal of area 41×57 μm^2. Sample thicknesses were estimated as 5 μm.

Low temperatures were reached using a He cold-finger cryostat attached to a solid copper block, which encapsulates the membrane-driven DAC [31]. Sample temperatures were estimated as the average value of the readings of two DT-670 Silicon diodes, one located at the bottom and one attached to the side of the copper block. Diffraction data were collected upon compression by rotating the sample together with the cryostat about the vertical ω axis. Pressures were measured by an online ruby fluorescence system [31–33].

A detailed description of the experimental setup is given in Refs. [22,31]. Information on the data collection and processing strategy (rotational range, exposure times, merging of runs, treatment special to HP data) can be found in Ref. [34]. The diffraction data were processed and analysed with aid of the software CRYSALISPRO [35] (for lattice parameters, **q**-vector components, integrated intensities) and JANA2006 [36] (for structure refinements, calculation of distances and angles, *t* plots).

C. Identification of phase transitions by SXRD

The orthorhombic-to-monoclinic lattice distortion is characteristic for the paramagnetic-to-antiferromagnetic phase transition in CrOCl, because of the strong magnetoelastic coupling in this compound [5,6,9]. Three aspects of the x-ray diffraction can be evaluated towards establishing the phase transitions.

Firstly, symmetry breaking at phase transitions may lead to twinned crystals. For small lattice distortions, as in *M*OCl, this pseudomerohedral twinning may become visible as split reflections in the SXRD. For an orthorhombic high-symmetry phase particularly, split reflections $(0\ k\ l)$ with different scattering angles 2θ indicate that $\alpha \neq 90$ deg for the low-symmetry phase [$(0\ k\ l)$ and $(0\ \bar{k}\ l)$ of the monoclinic or triclinic phases possess different scattering angles 2θ for $\alpha \neq 90$ deg]. Similarly, split into the 2θ direction of reflections $(h\ 0\ l)$ indicate $\beta \neq 90$ deg, and of reflections $(h\ k\ 0)$ indicate $\gamma \neq 90$ deg. Indeed, we observed at higher pressures a splitting of reflections for both 35 and 14 K (Figs. S1 and S2 in Ref. [34]). However, some of the observed splittings cannot be explained by lattice distortions arising from phase transitions. For example, reflections $(\bar{4}\ 0\ 0)$ and $(0\ \bar{4}\ 0)$ each have one length of the scattering vector in all possible domains (one value of 2θ). Nevertheless, the SXRD shows two maxima with different values of 2θ at pressures above 9.8 GPa. Such a splitting cannot be explained by twinning of a lower-symmetry lattice. Instead, it is indicative of two different values of *a* and two different values of *b* for the $(\bar{4}\ 0\ 0)$ and $(0\ \bar{4}\ 0)$ reflections, respectively. The presence of two or more domains at these pressures may be the result of

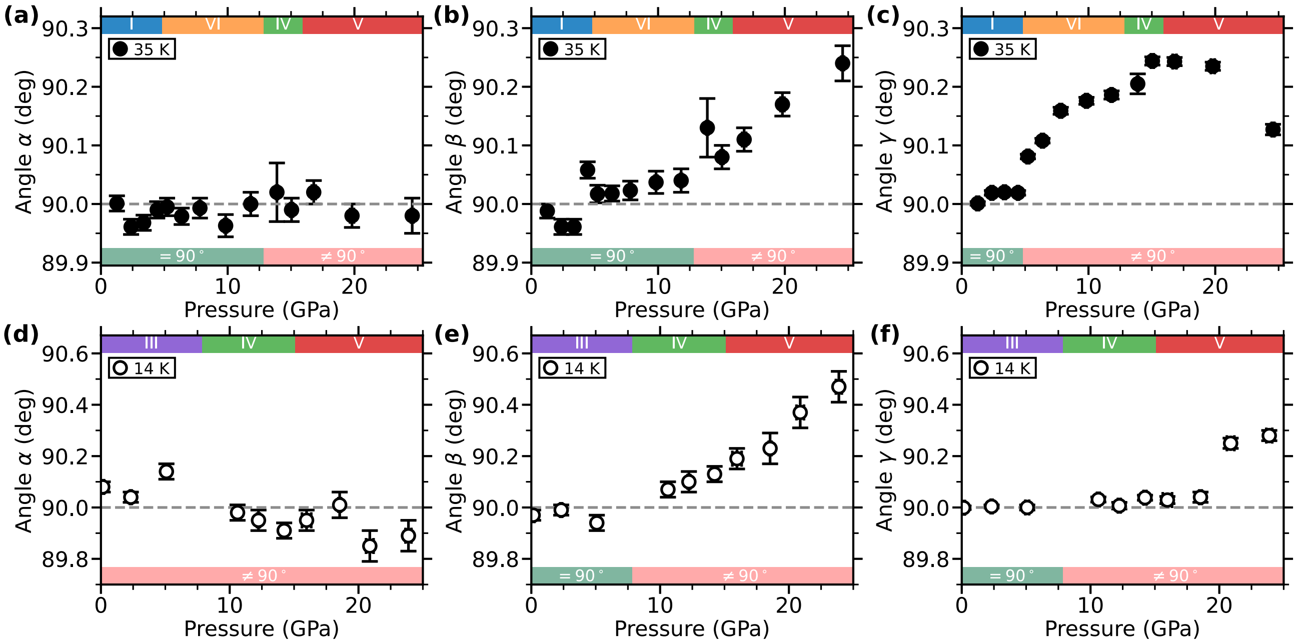

FIG. 2. Lattice parameter angles for 0–25 GPa at [(a)–(c)] $T = 35$ and [(d)–(f)] $T = 14$ K. No restrictions were applied to the lattice parameters during their refinement against the SXRD data. Dashed horizontal lines are at 90°. The lower bars indicate the combinations (p, T) for which the angle is either equal to 90° (light green color) or different from 90° (light red color; see text for details). The bars at the top of the panels indicate the phase diagram at $T = 35$ and 14 K, respectively (see also Fig. 3).

nonhydrostatic conditions inside the DAC, and this splitting does not bear any relation to the phase transitions. Furthermore, we believe that quite many of the measured SXRD data sets involve but one domain, since the x-ray beam has a small size below 8 μm. Therefore analyzing peak splittings does not lead to the correct symmetries in the present experiment.

Secondly, the unconstrained indexing of the measured SXRD data provides values for the lattice parameters. In particular, the angles α, β, and γ may help to distinguish orthorhombic symmetry (all angles equal to 90°) from monoclinic symmetry (one angle different from 90°) and triclinic symmetry (two or three angles different from 90°). If the

TABLE I. The (p, T) phase diagram of CrOCl. Phases are numbered with Roman numerals (compare to Fig. 3). Indicated are the lattice symmetry, the (super)space group SSG [37,38], the magnetic ($\mathbf{q}_M$) and nuclear ($\mathbf{q}_X$) modulation wave vectors, and the pressure range where each phase was observed. Phases IV, V, and VI are first reported in this study. Data at 293 K from Ref. [25].

					observed pressure range (GPa)		
Phase	Lattice	SSG	$\mathbf{q}_M$	$\mathbf{q}_X$	293 K	35 K	14 K
I	orthorhombic	59 $Pmmn$	–	–	$0 < p < 14.5$	$0 < p < 4.4(1)$	–
II[a]	orthorhombic	59.1.9.3 $Pmmn(0, \beta, 0)s0s$	$(0, \sigma_2, 0)$	n.o.	–	–	–
III[b]	monoclinic	59.1.9.3 $Pmmn(0, \beta, 0)s0s$	$(0, 1/4, 0)$	$(0, 1/2, 0)$	–	–	$0 < p < 5.1(2)$
IV	triclinic	2 $P\bar{1}$	n.o.	n.o.	–	$13.9(1) < p < 15.0(2)$	$10.6(1) < p < 14.2(2)$
V	triclinic	2.1.1.1 $P\bar{1}(\alpha, \beta, \gamma)0$	n.o.	$(\sigma_1, 0, \sigma_3)$	–	$16.8(2) < p < 46.7(1)$	$16.0(4) < p < 37.0(3)$
VI	monoclinic	13 $P112/n$	n.o.	n.o.	–	$5.2(1) < p < 11.8(1)$	–
VII	orthorhombic	59.1.10.6 $Pmmn(\alpha, 0, 1/2)00s$	–	$(\sigma_1, 0, 1/2)$	$16.4 < p < 51.0$	–	–
VIII[c]	orthorhombic	59.1.10.6 $Pmmn(\alpha, 0, 1/2)00s$	–	$(1/3, 0, 1/2)$	$p = 57.2$	–	–
IX[c]	monoclinic	11 $P12_1/m1$	–	$(1/3, 0, 1/3)$	$p = 57.2$	–	–

[a] Phase II occurs for $13.5 < T < 27$ K at ambient pressure, with a magnetic modulation wave vector $\sigma_2 \approx 0.2403(2) - 0.000048(8)\,T$; no satellite reflections in x-ray diffraction [5–7,9].

[b] Magnetic and nuclear modulations are related through $\mathbf{q}_X = 2\,\mathbf{q}_M$. The supercell is **a**-unique monoclinic [5–7]; satellites are not observed in the present HPLT experiment.

[c] Coexisting phases VIII and IX at $p = 57.2$ GPa; phase VIII survived decompression down to $p = 47.5$ GPa [25].

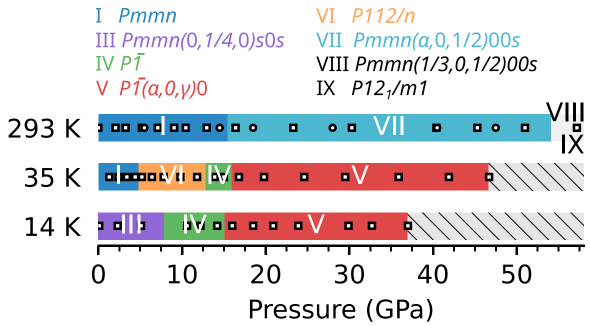

FIG. 3. Schematic representation of the (p, T)-phase diagram of CrOCl at $T = 293$ K (data taken from Ref. [25]), and $T = 35$ and 14 K (this study) (see also Table I). The (super)space group assignment is given at the top of the diagram. Phase II (occuring between 13.5 and 27.2 K at 1 bar [5]) is omitted here, since it has not been observed within the currently reported (p, T) range. Each measured (p, T) combination is indicated by either a square marker (measured on compression) or a circle (measured on decompression). No data is available for the hatched pressure ranges. The bar diagrams for $T = 35$ and 14 K are used in Figs. 2, 4, 6, 7, 8, and 10.

SXRD data originate from a single domain, the unconstrained indexing should provide the correct lattice parameters, and thus provide evidence for the correct lattice symmetry. However, this analysis is complicated by the lack of accuracy of the lattice parameters derived from HP SXRD, because of the highly incomplete data sets, possibly inhomogeneous pressure and possible misalignments of sample and rotation axis. In case of CrOCl, an additional complication arises from the platelet-like habit of the single crystal, which causes the large (0 0 1) crystal facets to be parallel with the diamond culets. With the limited range of sample rotation, immanent to the DAC technique, this configuration leads to a reduced accuracy of the angles α and β, while γ is the most accurately measured angle (Fig. 2).

At $T = 35$ K, the results of our analysis provide strong evidence for an orthorhombic to **c**-unique monoclinic phase transition at a critical pressure p_c with $4.4 < p_c < 5.2$ GPa (Fig. 2, Fig. 3 and Table I). It is noticed that at 35 K, Neon solidifies below 0.1 GPa [39]. The observed phase transitions with critical pressures $p_c > 4.4$ GPa can thus be attributed to phase transitions of CrOCl, and they are not related to the pressure transmitting medium. A transition towards phase IV with triclinic symmetry takes place at a critical pressure with $11.8 < p_c < 13.9$ GPa. The presence of satellite reflections with $\mathbf{q}_X = [0.287(1),\ 0.000(1),\ 0.496(1)]$ in the SXRD at 16.8 GPa indicates the transition towards the triclinic phase V at a critical pressure with $15.0 < p_c < 16.8$ GPa (see Fig. S18 in Ref. [34]).

The situation is less clear at $T = 14$ K. At ambient pressure and LT conditions, SXRD has led to $\alpha = 90.05^\circ$ below 14 K [5]. This deviation from 90° lies within the uncertainty of α in the present HPLT experiment, and the latter does not necessarily provide evidence for a significant deviation from 90° of the angle α for all pressures 0–24 GPa [Figs. 2(d), S17(d), and 17(j)]. However, supported by the observations reported in [5], we assume that $\alpha \neq 90^\circ$ for all pressures at 14 K. The transition from monoclinic phase III towards triclinic phase IV then is found for $5.1 < p_c < 10.6$ GPa [Fig. 2(e) and Table I].

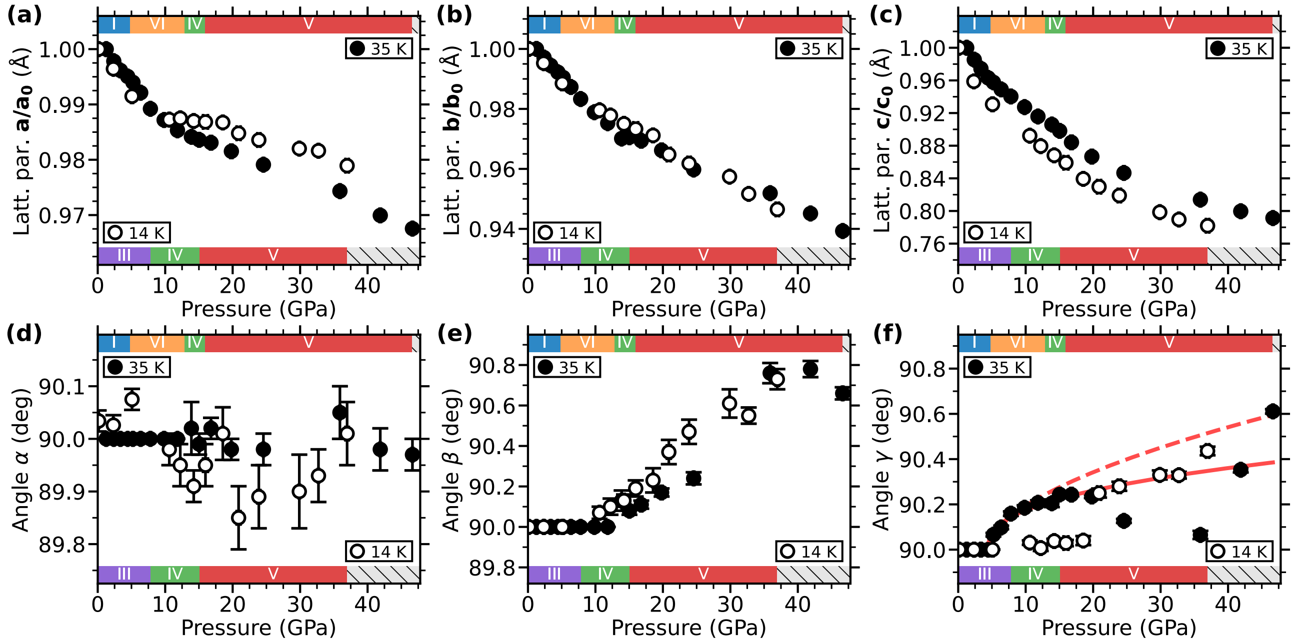

FIG. 4. Lattice parameters as a function of pressure for $T = 35$ K (closed circles) and $T = 14$ K (open circles). [(a)–(c)] Normalized lattice parameters a/a_0, b/b_0 and c/c_0, with $a_0(35) = 3.85074(14)$ Å, $a_0(14) = 3.85350(17)$ Å, $b_0(35) = 3.16507(12)$ Å, $b_0(14) = 3.16950(16)$ Å, $c_0(35) = 7.453(5)$ Å, and $c_0(14) = 7.6964(70)$ Å. [(d)–(f] Lattice parameter angles α, β and γ. Values have been obtained from constrained refinements against the SXRD data. The phase diagram at $T = 35$ and $T = 14$ K are indicated at the top and bottom of each panel, respectively (compare to Fig. 3). The pressure-dependent values of γ have been fitted by Eq. (1) for $4.4 \leqslant p \leqslant 19.8$ GPa (solid line; $\beta_c = 0.39(5)$ and $p_c = 4.4(1)$ GPa) and for $4.4 \leqslant p \leqslant 9.8$ GPa (dashed line; $\beta_c = 0.56(8)$ and $p_c = 4.4(1)$ GPa).

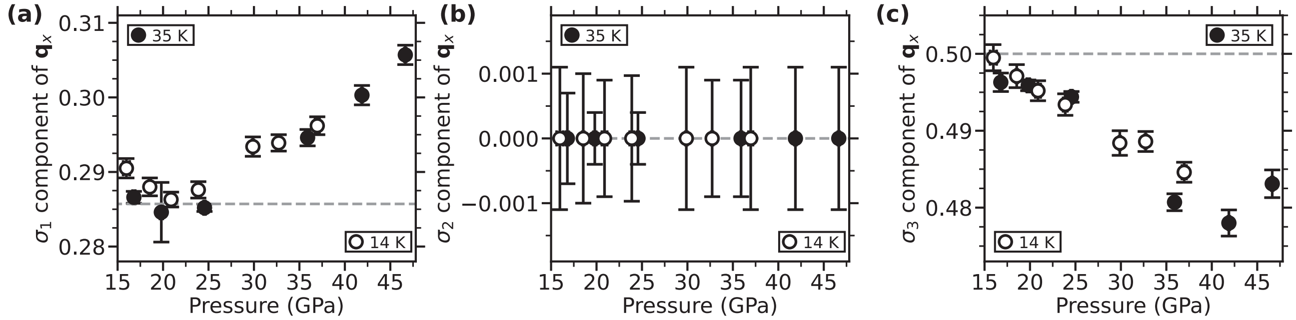

FIG. 5. Pressure dependence of the components of the modulation wave vector $\mathbf{q}_X = (\sigma_1, \sigma_2, \sigma_3)$ for $T = 35$ K (filled circles) and $T = 14$ K (open circles). (a) σ_1 (dashed line at 2/7), (b) σ_2 (dashed line at 0) and (c) σ_3 (dashed line at 1/2). Satellite reflections have been observed for $p > 15$ GPa. All (p, T) combinations are within triclinic phase V (compare to Table I).

The transition to the triclinic phase V takes place at a critical pressure of value $14.2 < p_c < 16.0$ GPa, as it is evidenced by the presence of satellite reflections in the diffraction at 16.0 GPa.

Thirdly, for each data set, structure refinements have been performed under the assumption of different symmetries. The best fit then would indicate the correct structure model. However, in many cases models of different symmetries provide fits to the data of almost equal quality. The present HP SXRD data were averaged according to Laue symmetry $\bar{1}$. Irrespective of the structure model, the atomic displacement parameters (ADPs) were restricted according to *Pmmn* symmetry. Refinements were carried out in *Pmmn* and its subgroups $P2_1/m11$, $P12_1/m1$, $P112/n$, and $P\bar{1}$. If satellite reflections were observed, the corresponding superspace groups were used as symmetry, and the structure model was expanded by modulation parameters.

For most data sets, the fits to the data are of similar quality for the different symmetries (Table S2 in Ref. [34]). It follows that model comparisons are not a suitable method for distinguishing the different symmetries in the present case.

D. Structural parameters in dependence on pressure and temperature

The phase boundaries and the correct symmetries of the different phases have been determined on the basis of a combined analysis of pressure dependent lattice parameters (Figs. 2 and S17), the presence or absence of satellite reflections, and structure refinements (Table S2 in Ref. [34]). After having done so, lattice parameters were obtained by constrained refinements against the SXRD, according to the appropriate orthorhombic, monoclinic or triclinic symmetries, as they are defined in Table I (Fig. 4). The same refinements then provide the components of the modulation wave vector (Fig. 5). It is stressed that satellite reflections have only been observed for pressures higher than 15 GPa. The appearance of these satellites upon compression is one major criterion signaling the transition from triclinic phase IV to triclinic phase V (Fig. S18 in Ref. [34]).

Employing these lattice parameters, structure refinements were performed within the appropriate space group or superspace group symmetry. It should be noted, that structure refinements are very similar for the two sets of lattice parameters (Figs. 2, S17, and 4), but that even a small difference in lattice parameters directly translates into different values for interatomic distances and angles.

At each (p, T) combination, the volume of the unit cell has been computed from the lattice parameters. It exhibits a smooth dependence on pressure across multiple phase transitions, with nearly identical curves at 14 and 35 K (Fig. 6). The volume-vs-pressure data have been fitted by a third-order Birch-Murnaghan equation of state (BM-EOS) [40,41]. Separate BM-EOS have been determined for 14 and 35 K, but the fit employed data points across all phase transitions. Similar values were obtained at each temperature for the zero-pressure volume V_0, the bulk modulus K_0, and its derivative K' (Table II).The lowest pressure at 14 K was not used in the fit, in order to obtain matching pressure ranges for the different temperatures.

III. DISCUSSION

A. The high-pressure–low-temperature phase diagram

CrOCl is paramagnetic at ambient conditions with an orthorhombic crystal structure in *Pmmn* (phase I, see Table I) [27]. Upon cooling, incommensurate magnetic order develops

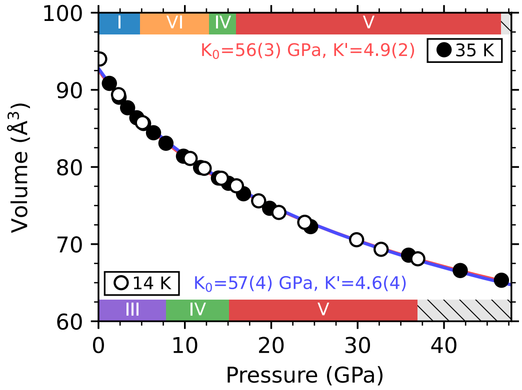

FIG. 6. Pressure dependence of the volume of the unit cell at 35 K (filled circles) and 14 K (open circles). Lines represent fits to the data points with the BM-EOS [40,41] using the software EOSFIT7-GUI [42]. The upper bar indicates the phase diagram at $T = 35$ K and the lower bar at $T = 14$ K (see also Fig. 3). An expanded view of the (p, V) diagram for $0 < p < 20$ GPa is given in Fig. S16 [34].

TABLE II. Parameters obtained from BM-EOS [40,41] fits of p-V at $T = 293$ K (with data from Ref. [25]), $T = 35$ K, and $T = 14$ K using the software EOSFIT7-GUI [42]. BM-EOS fits at 14 and 293 K are given for full pressure ranges (all measured data points) and for pressure ranges without the lowest pressure data. The latter fits are provided for a better comparison with the more limited data available for 35 K. For the purpose of comparison, BM-EOS fits are provided for pressure ranges with similar starting pressures between 1.3 and 2.3 GPa for all three temperatures.

T (K)	range (GPa)	V_0 (Å^3)	K_0 (GPa)	K’
293[a]	2.1–51.0	93.4(5)	48(6)	5.7(9)
293[a]	1×10^{-4}–51.0	94.4(3)	38(3)	7.4(1.0)
35	1.3–46.7	92.6(3)	56(3)	4.9(2)
14	2.3–37.0	92.8(5)	57(4)	4.6(4)
14	0.1–37.0	93.8(3)	49(3)	5.3(4)

[a] A fit with a third-order Vinet EOS [43] leads, within the estimated uncertainties, to similar results.

below $T_c = 27.2$ K (phase II), which is followed by a first-order phase transition at $T_N = 13.5$ K, that leads to an AFM phase with a fourfold magnetic supercell (phase III) [5,6,23]. The incommensurate AFM phase is orthorhombic and it has an incommensurate magnetic propagation vector, but it does not lead to any satellite reflections in the x-ray diffraction. Magnetic order in phase III is facilitated by a monoclinic lattice distortion with $\alpha \approx 90.05^\circ$ [5]. The presence of satellite reflections in the x-ray diffraction reflect a superstructure corresponding to a fourfold magnetic superstructure (Table I). They are the result of strong magnetoelastic coupling.

The present experiment involves pressure-dependent x-ray diffraction at temperatures just above T_c and just above T_N. Unfortunately, no satellite reflections could be observed that would correspond to the magnetoelastic coupling. Most probably they are not observed, because of the high background in HPLT diffraction experiments, which obliterates weak satellite reflections. Nevertheless, by argument of continuity, we believe that at 14 K phase III exists up to a pressure of at least 5.1 GPa. This feature is similar to the observations for FeOCl, where the AFM phase was found to persist up to ∼ 14 GPa at low temperatures, although satellite reflections could not be observed [22].

At 35 K (above T_c), the paramagnetic, orthorhombic phase I remains stable up to 4.4 GPa. It is followed by a transition at $4.4 < p_c < 5.2$ GPa towards a **c**-unique monoclinic state (phase VI). Phase VI has the same lattice symmetry as that of the AFM phases of FeOCl and VOCl, and thus is a candidate for AFM order in CrOCl. However, the AFM phase of CrOCl at low temperatures is **a**-unique monoclinic (phase III).

Further increase of pressure results in transitions to phase IV with $5.1 < p_c < 10.6$ GPa at 14 K, and $11.8 < p_c < 13.9$ GPa at 35 K. Since at 14 K the crystal is already in the monoclinic AFM phase III at lower pressures, the formation of triclinic phase IV might have a pure structural origin at both 14 and 35 K. The transition to triclinic phase V takes place at $14.2 < p_c < 16.0$ GPa at 14 K, and $15.0 < p_c < 16.8$ GPa at 35 K. This transition is established through the appearance of satellite reflections that reflect the structural modulation that was previously reported as phase VII at room temperature (Table I). The structural transition involves optimization of the packing of chlorine atoms within the van der Waals gap, and it typically occurs, when the Cl $\cdots$ Cl distances across the van der Waals gap fall below ∼3 Å [25]. The present results indicate that this happens at 14 and 35 K at about the same pressure as at 293 K and at about the same pressure as for FeOCl (Fig. 7) [22,25]. Our observations suggest that the transitions towards the structurally modulated phases take place at critical pressures that are temperature independent to a first approximation.

B. Compressibility and phase transitions

The pressure dependence of the specific volume of CrOCl at 14 and 35 K exhibits a smooth progression across multiple phase transitions (Fig. 6), which has been described by a single BM-EOS at each of the two temperatures (Table II). The bulk modulus depends on the pressure range used for

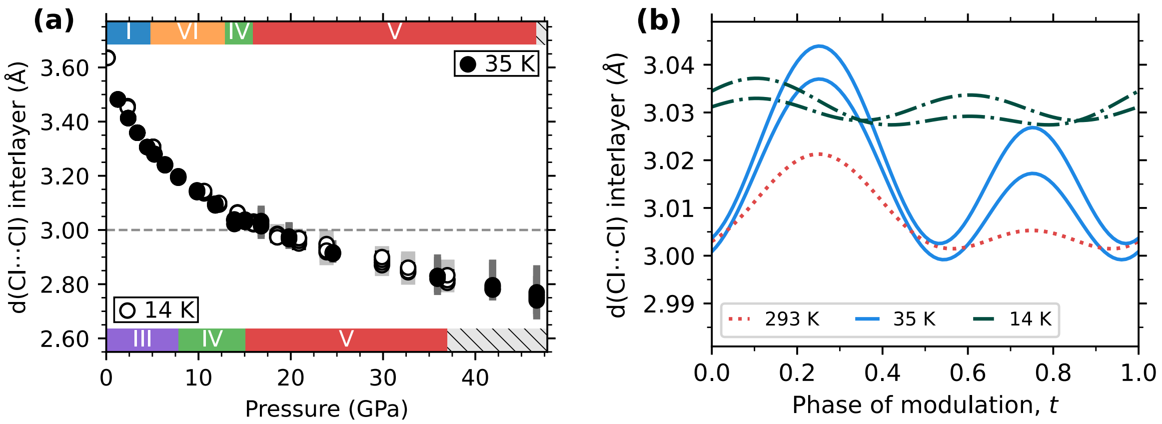

FIG. 7. (a) Cl $\cdots$ Cl interlayer distances as a function of pressure for $T = 35$ K (filled circles) and $T = 14$ K (open circles). The upper bar indicates the phase diagram at $T = 35$ K and the lower bar at $T = 14$ K (compare to Fig. 3). The dashed horizontal line marks the value of 3 Å. Two nearly equal Cl $\cdots$ Cl distances exist at each pressure in the monoclinic phases III and VI and four such distances exist in the triclinic phases IV and V. Light-gray (14 K) and dark-gray (35 K) bars reflect the range of values in the modulated phase V. (b) t-plot of the Cl $\cdots$ Cl interlayer distance at 293 K/16.4 GPa (orthorhombic; data from Ref. [25]), 35 K/16.8 GPa (triclinic), and 14 K/16.0 GPa (triclinic).

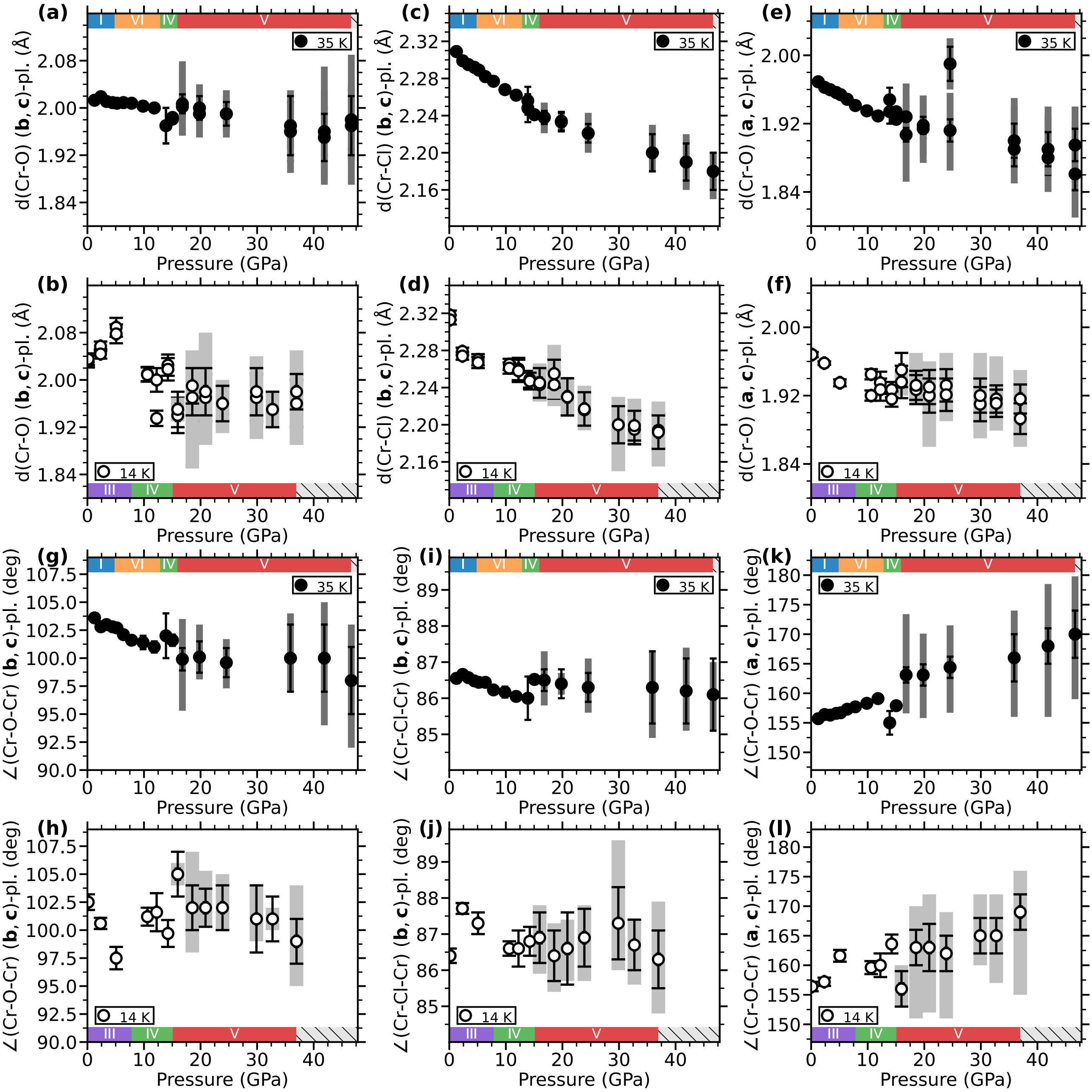

FIG. 8. Selected interatomic distances and bond angles as a function of pressure for $T = 35$ K (filled circles) and $T = 14$ K (open circles). [(a) and (b)] Cr–O distances within CrOCl ribbons parallel to the (**b**, **c**) plane; [(c) and (d)] Cr–Cl distances within ribbons; [(e) and (f)] Cr–O distances between ribbons; [(g) and (h)] Cr–O–Cr angle within ribbons; [(i) and (j)] Cr–Cl–Cr angle within ribbons; and [(k) and (l)] Cr–O–Cr angle along **a**. Vertical gray bars encompass the ranges of values present in the structurally modulated phase V, with the associated symbol indicating the average value. Each bond or angle in orthorhombic phase I splits into two or four closely separated values in the monoclinic and triclinic phases, respectively. The upper bar indicates the phase diagram at $T = 35$ K and the lower bar at $T = 14$ K (compare to Fig. 3).

the fit procedure. With similar ranges, the bulk moduli can not be distinguished from each other at 14 and 35 K. Despite large standard uncertainties, the data suggest that K_0 is slightly smaller at 293 K than at low temperatures (Table II). FeOCl has bulk moduli of $K_0 = 36(3)$ GPa at 293 K, $K_0 = 39(3)$ GPa at 100 K and $K_0 = 45(3)$ GPa at 6 K [22,44]. According to these values, CrOCl appears to be less compressible than FeOCl. Such different behavior can be understood on the basis of interatomic distances: Cr–O bonds are shorter than Fe–O bonds and the layers are therefore less compressible. On the other hand, the Cl···Cl interlayer contacts have equal length and equal pressure dependence for CrOCl and FeOCl (Fig. S14 in Ref. [34]), and thus explain similar critical pressures for the transitions to the structurally modulated phases.

The compressibility of *M*OCl is in general highly anisotropic, with the largest effect at lower pressures being a reduction of the width of the van der Waals gap between the layers. We have found this observation to be true also for CrOCl at low temperatures (Fig. S13). Apart from this anisotropy, the pressure dependence of individual lattice parameters is irregular with anomalies observed at the phase transitions (Fig. 2). This is again similar behavior as for FeOCl (Fig. S13). The apparent anomalies in, especially, a coincide with anomalies in the angles β and γ, the latter which are the result of the reduction of lattice symmetry to monoclinic and triclinic. Therefore the anomaly in the length a is the result of a rotation of the basis vector **a**, while a smooth pressure dependence remains for the perpendicular distances [22].

The limited accuracy and the limited number of data points prohibit the determination of the character of most of the observed phase transitions. Nevertheless, group-theoretical considerations show that both $P2/n$ (**c** unique) and $P2_1/m$ (**a** unique) can be reached through continuous phase transitions [45]. Furthermore, continuous phase transitions might take place involving the appearance of structural or magnetic modulations according to incommensurate wave vectors (Table I). At 35 K, the deviation from 90° of γ exhibits a smooth increase into the monoclinic phase VI [Fig. 2(f)]. Following Ref. [22], this dependence has been described as critical behavior with $(\gamma - 90^\circ)$ as order parameter,

$$\gamma - 90^\circ = A(p - p_c)^{\beta_c}, \qquad (1)$$

where A is an amplitude, and p_c is the critical pressure and β_c is the critical exponent of the second-order phase transition. A fit to the data for $4.4 \leqslant p \leqslant 19.8$ GPa results in $\beta_c = 0.39\ (5)$. Employing data for $4.4 \leqslant p \leqslant 9.8$ GPa results in $\beta_c = 0.56\ (8)$. A critical pressure of $p_c = 4.4(1)$ GPa has been obtained in both cases. The critical function [Eq. (1)] should describe behavior close to p_c. On the other hand, large uncertainties are obtained for β_c, if only the few data points close to p_c are used for the fit. Accordingly, both values obtained for β_c posses large standard uncertainties, and the values are within the realm of the 3D Ising, the XY, the Heisenberg and the mean-field models for second-order phase transitions [22,46].

At room temperature, the structurally modulated phase evolves from the paramagnetic phase of CrOCl and FeOCl and it retains orthorhombic symmetry (phase VII) [25]. At low temperatures, the structural modulation appears in the AFM phase of FeOCl and retains its monoclinic symmetry. For CrOCl we presently find that the structural modulation develops in the AFM phase, after the crystal symmetry has become triclinic (phase IV). Accordingly, the structurally modulated phase V retains the triclinic symmetry. The different symmetries of orthorhombic phase VII and triclinic phase V thus appear to be the result of the symmetry of the parent phase just below the critical pressure. To a first approximation, the structural modulation itself remains compatible with orthorhombic symmetry at all three temperatures. This conclusion is supported by the values of the component σ_1 of the modulation wave vector and the magnitudes of the interatomic distances, which exhibit similar pressure dependencies for phases V and VII (Fig. 5, Fig. 8, and Sec. S5 in Ref. [34]). The reduction towards triclinic symmetry appears to be decoupled from the structural modulation. Introducing additional lattice and structural degrees of freedom may lead to more favorable distortions than is provided by further contraction of the Cr–O and Cr–Cl bonds in high-symmetry structures. The presence of triclinic lattice distortions in both CrOCl and FeOCl at high pressures and low temperatures suggests that this distortion could be a general mechanism for accommodating high pressure in the FeOCl structure type.

C. Consequences of structural distortions for the magnetic interactions

The present HPLT diffraction experiments provide only indirect evidence for magnetic order at elevated pressures. At 14 K, the argument of continuity is employed to assign commensurate AFM order to the monoclinic crystal structure (phase III). It is not unlikely that this magnetic order pertains into phases IV and V. However, the structural distortions do affect any magnetic exchange interactions with ramifications for the type of magnetic order in the high-pressure phases.

Three main types of exchange interactions have been identified in the orthorhombic crystal structure of CrOCl: J_1 for AFM coupling between Cr^{3+} ions of neighboring ribbons; J_2 for AFM coupling on the Cr chains along **b**; and J_3 for ferromagnetic coupling along **a** (Fig. 9) [10]. Frustration of AFM order is governed by the four equivalent J_1 contacts of each Cr^{3+} ion. In case of an **a**-unique monoclinic distortion, frustration is lifted by $J_a = J_c$ becoming independent from $J_b = J_d$. In case of an **c**-unique monoclinic distortion, frustration is lifted by $J_a = J_d \neq J_b = J_c$ (Fig. 9).

The present HPLT data indicate values of α of the same order of magnitude as previously obtained at low temperatures and ambient pressure [5]. Larger distortions that increase with increasing pressure, are, however, found for the angles β and γ (Fig. 4). The triclinic phase thus features four independent exchange parameters, J_a, J_d, J_b and J_c, replacing J_1. Indeed, the four short Cr–Cr contacts between ribbons at $(\pm\mathbf{a} \pm \mathbf{b})/2$ split into two (phases III and VI) or four (phases IV and V) different distances, with a difference that increases

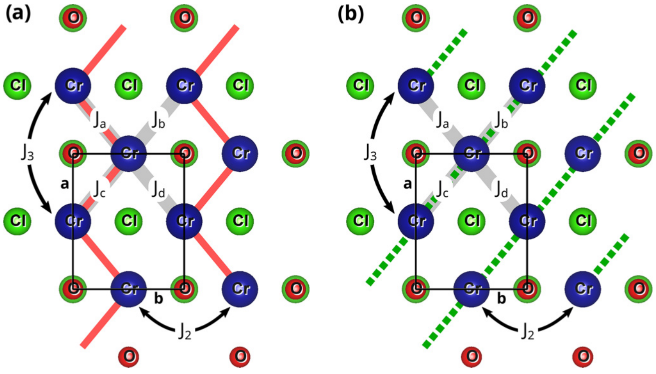

FIG. 9. Projection of one layer CrOCl onto the (**a**, **b**) plane. Black lines denote the unit cell of the basic structure. Exchange parameters according to Refs. [5,10] are indicated by J_2, J_3 and $J_1 = J_a = J_b = J_c = J_d$. These equalities represent the frustration for AFM order within orthorhombic symmetry. (a) For an **a**-unique monoclinic distortion, diagonal Cr–Cr distances are shorter along the red lines, and frustration is lifted as $J_a = J_c \neq J_b = J_d$. (b) For an **c**-unique monoclinic distortion, dashed green lines indicate the shorter Cr–Cr contacts, and $J_a = J_d \neq J_b = J_c$.

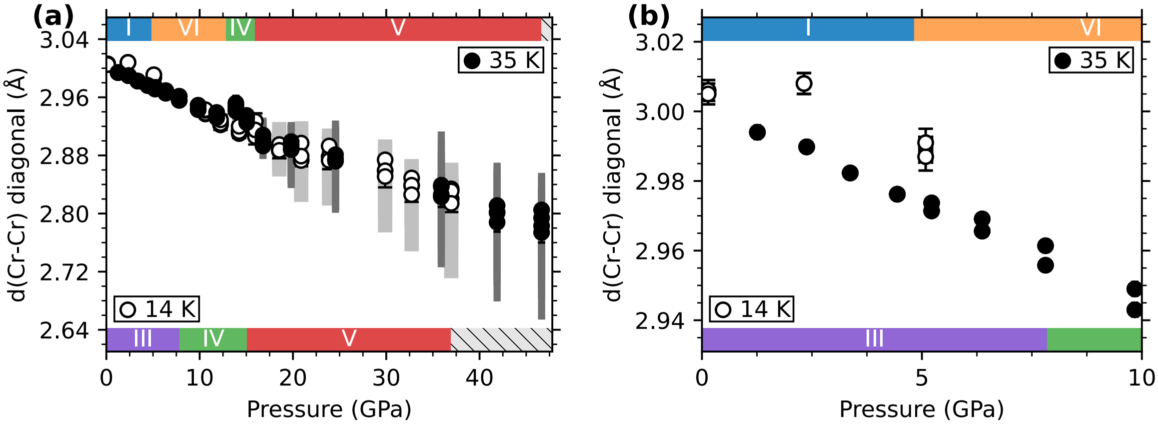

FIG. 10. Short Cr–Cr distances between ribbons as a function of pressure for $T = 35$ K (filled circles) and $T = 14$ K (open circles). (a) Full pressure range, and (b) expanded view for 0–10 GPa. Vertical dark gray and light gray ribbons indicate the range of values in the structurally modulated phase V. Up to four independent contacts are displayed, depending on the symmetry. The upper bar indicates the phase diagram at $T = 35$ K and the lower bar at $T = 14$ K (see also Fig. 3).

with pressure (Fig. 10). In general, Cr–O–Cr bond angles and Cr–O bond lengths show a strong pressure dependence (Fig. 8). Accordingly, magnetic interactions can be expected to be strongly pressure dependent, with variations of direct exchange and superexchange interactions that cannot be easily predicted on the basis of the geometries of the crystal structures.

Previously, it was argued that the **c**-unique monoclinic distortion is less effective than the **a**-unique monoclinic distortion for removing the frustration for AFM order in CrOCl, because of the symmetries of the occupied 3*d* orbitals [5]. In view of this argument and the observation that incommensurate magnetic order does not require removal of the frustration, it is possible that phase VI involves incommensurate magnetic order that is similar to the incommensurate magnetic order of phase II at low temperatures and ambient pressure. A lower bound for the pressure dependence of this transition then is $\Delta T_c/\Delta p = 1.42$ K/GPa, which is a reasonable value. Alternatively, if phase VI would involve commensurate magnetic order, the pressure coefficient would be $\Delta T_N/\Delta p = 4.1$ K/GPa. This value is twice as large as for FeOCl [22], but it is comparable to the pressure coefficient of the Néel temperature of MnO [47].

IV. CONCLUSIONS

CrOCl is a quasi-two-dimensional van der Waals magnet. Within the orthorhombic symmetry, Cr^{3+} ions of one layer are at the nodes of a triangular lattice. This explains that antiferromagnetic (AFM) order is frustrated for orthorhombic CrOCl. Lattice distortions may lift this frustration (Fig. 9), but orbital order with three filled 3*d* orbitals makes this less effective for CrOCl than for FeOCl or VOCl, which becomes apparent by the large differences of the Néel temperature of $T_{N,1\mathrm{bar}} = 13.5 - 14.0$ K in CrOCl, $T_{N,1\mathrm{bar}} = 81.0(2)$ K in FeOCl and $T_{N,1\mathrm{bar}} = 80.0(3)$ K in VOCl [5–7,46,48].

Diffraction experiments have revealed three new high-pressure phases of CrOCl. Phase VI at 35 K above $T_c = 27$ K possess **c**-unique monoclinic symmetry. It is argued that phase VI might be a high-pressure counterpart of the incommensurately modulated AFM phase (orthorhombic phase II), stable below T_c at ambient pressure [6]. Alternatively, it could be the high-pressure counterpart of the commensurate AFM phase (phase III), stable below $T_N = 13.5$ K at ambient pressure, which has **a**-unique monoclinic symmetry [5].

At yet higher pressures, a triclinic lattice distortion is present (phase IV), which develops a structural modulation (phase V) for pressures larger than p_c with $15.0 < p_c < 16.0$ GPa. Phase V is the low-temperature counterpart of the structurally modulated phase VII that appears at room temperature at a similar pressure p_c and has orthorhombic symmetry. Modulations are responsible for the optimization of the packing of Cl atoms within the van der Waals gap. Despite different symmetries, the modulations are similar in phases V and VII.

A counterpart of triclinic phase V was not found at room temperature. The reduction towards triclinic symmetry—with or without AFM order (see above)—is decoupled from the structural modulation. It may involve more favorable distortions than is provided by further contraction of the Cr–O and Cr–Cl bonds in high-symmetry structures, since these bonds are already shorter due to the thermal expansion between 35 and 293 K.

ACKNOWLEDGMENTS

Single crystals were synthesized by Kerstin Küspert at the Laboratory of Crystallography in Bayreuth. We acknowledge DESY (Hamburg, Germany), a member of the Helmholtz Association HGF, for the provision of experimental facilities. Parts of this research were carried out at PETRA III, using beamline P02.2. Beam time was allocated for Proposal No. I-20190296. We thank H.-P. Liermann for support of our experiment. This research has been funded by the Deutsche Forschungsgemeinschaft (DFG; German Research Foundation)–386411512.

[1] S. Yang, T. Zhang, and C. Jiang, Van der Waals magnets: Material family, detection and modulation of magnetism, and perspective in spintronics, Adv. Sci. **8**, 2002488 (2021).

[2] M.-C. Wang, C.-C. Huang, C.-H. Cheung, C.-Y. Chen, S. G. Tan, T.-W. Huang, Y. Zhao, Y. Zhao, G. Wu, Y.-P. Feng, H.-C. Wu, and C.-R. Chang, Prospects and opportunities of 2D van der Waals magnetic systems, Ann. Phys. **532**, 1900452 (2020).

[3] H. Li, S. Ruan, and Y.-J. Zeng, Intrinsic van der Waals magnetic materials from bulk to the 2D limit: New frontiers of spintronics, Adv. Mater. **31**, 1900065 (2019).

[4] K. S. Burch, D. Mandrus, and J.-G. Park, Magnetism in two-dimensional van der Waals materials, Nature (London) **563**, 47 (2018).

[5] J. Angelkort, A. Wölfel, A. Schönleber, S. van Smaalen, and R. K. Kremer, Observation of strong magnetoelastic coupling in a first-order phase transition of CrOCl, Phys. Rev. B **80**, 144416 (2009).

[6] J. Zhang, Temperature dependent magnetic order in FeOCl type compounds, Ph.D. thesis, Universität Bayreuth (2014)

[7] P. G. Reuvekamp, Investigation into the magnetic and the structural properties of two low-dimensional antiferromagnets $TiPO_4$ and CrOCl, Ph.D. thesis, Universität Stuttgart, Stuttgart (2014).

[8] B. Das, S. Ghosh, T. Kundu, R. Paramanik, S. Maity, M. Palit, S. Das, P. Kumar Hazra, P. Maji, A. Ghosh, and S. Datta, Metamagnetism and magnetocaloric properties in a van der waals antiferromagnet CrOCl, Physica Status Solidi (b) **260**, 2200422 (2023).

[9] P. Gu, Y. Sun, C. Wang, Y. Peng, Y. Zhu, X. Cheng, K. Yuan, C. Lyu, X. Liu, Q. Tan, Q. Zhang, L. Gu, Z. Wang, H. Wang, Z. Han, K. Watanabe, T. Taniguchi, J. Yang, J. Zhang, W. Ji *et al.*, Magnetic phase transitions and magnetoelastic coupling in a two-dimensional stripy antiferromagnet, Nano Lett. **22**, 1233 (2022).

[10] S. W. Jang, D. H. Kiem, J. Lee, Y.-G. Kang, H. Yoon, and M. J. Han, Hund's physics and the magnetic ground state of CrOX (X = Cl, Br), Phys. Rev. Mater. **5**, 034409 (2021).

[11] K. Momma and F. Izumi, VESTA 3 for three-dimensional visualization of crystal, volumetric and morphology data, J. Appl. Crystallogr. **44**, 1272 (2011).

[12] T. Zhang, Y. Wang, H. Li, F. Zhong, J. Shi, M. Wu, Z. Sun, W. Shen, B. Wei, W. Hu, X. Liu, L. Huang, C. Hu, Z. Wang, C. Jiang, S. Yang, Q.-M. Zhang, and Z. Qu, Magnetism and optical anisotropy in van der waals antiferromagnetic insulator CrOCl, ACS Nano **13**, 11353 (2019).

[13] A. K. Nair, S. Rani, M. V. Kamalakar, and S. J. Ray, Bi-stimuli assisted engineering and control of magnetic phase in monolayer CrOCl, Phys. Chem. Chem. Phys. **22**, 12806 (2020).

[14] X. Qing, H. Li, C. Zhong, P. Zhou, Z. Dong, and J. Liu, Magnetism and spin exchange coupling in strained monolayer CrOCl, Phys. Chem. Chem. Phys. **22**, 17255 (2020).

[15] J. Cenker, S. Sivakumar, K. Xie, A. Miller, P. Thijssen, Z. Liu, A. Dismukes, J. Fonseca, E. Anderson, X. Zhu, X. Roy, D. Xiao, J.-H. Chu, T. Cao, and X. Xu, Reversible strain-induced magnetic phase transition in a van der Waals magnet, Nat. Nanotechnol. **17**, 256 (2022).

[16] Y. Wang, C. Wang, S.-J. Liang, Z. Ma, K. Xu, X. Liu, L. Zhang, A. S. Admasu, S.-W. Cheong, L. Wang, M. Chen, Z. Liu, B. Cheng, W. Ji, and F. Miao, Strain-sensitive magnetization reversal of a van der Waals magnet, Adv. Mater. **32**, 2004533 (2020).

[17] M. Pizzochero and O. V. Yazyev, Inducing magnetic phase transitions in monolayer CrI_3 via lattice deformations, J. Phys. Chem. C **124**, 7585 (2020).

[18] I. S. Lyubutin, S. S. Starchikov, A. G. Gavriliuk, I. A. Troyan, Y. A. Nikiforova, A. G. Ivanova, A. I. Chumakov, and R. Ruffer, Magnetic phase separation and strong enhancement of the Néel temperature at high pressures in a new multiferroic $Ba_3TaFe_3Si_2O_{14}$, JETP Lett. **105**, 26 (2017).

[19] Y. Sun, R. C. Xiao, G. T. Lin, R. R. Zhang, L. S. Ling, Z. W. Ma, X. Luo, W. J. Lu, Y. P. Sun, and Z. G. Sheng, Effects of hydrostatic pressure on spin-lattice coupling in two-dimensional ferromagnetic $Cr_2Ge_2Te_6$, Appl. Phys. Lett. **112**, 072409 (2018).

[20] A. S. Ahmad, Y. Liang, M. Dong, X. Zhou, L. Fang, Y. Xia, J. Dai, X. Yan, X. Yu, J. Dai, G.-J. Zhang, W. Zhang, Y. Zhao, and S. Wang, Pressure-driven switching of magnetism in layered $CrCl_3$, Nanoscale **12**, 22935 (2020).

[21] M. J. Coak, D. M. Jarvis, H. Hamidov, A. R. Wildes, J. A. M. Paddison, C. Liu, C. R. S. Haines, N. T. Dang, S. E. Kichanov, B. N. Savenko, S. Lee, M. Kratochvílová, S. Klotz, T. C. Hansen, D. P. Kozlenko, J.-G. Park, and S. S. Saxena, Emergent Magnetic Phases in Pressure-Tuned van Der Waals Antiferromagnet $FePS_3$, Phys. Rev. X **11**, 011024 (2021).

[22] A. M. Schaller, M. Bykov, E. Bykova, K. Glazyrin, and S. van Smaalen, Pressurizing the van der Waals magnet FeOCl at low temperatures: Phase transitions and structural evolution, Phys. Rev. B **105**, 184109 (2022).

[23] A. N. Christensen, T. Johansson, and S. Quezel, Preparation and magnetic properties of CrOCl, Acta Chem. Scand. A **28**, 1171 (1975).

[24] M. Zhang, Q. Hu, C. Hua, M. Cheng, Z. Liu, S. Song, F. Wang, P. He, G.-H. Cao, Z.-A. Xu, Y. Lu, J. Yang, and Y. Zheng, Metamagnetic transitions in few-layer CrOCl controlled by magnetic anisotropy flipping, arXiv:2108.02825.

[25] M. Bykov, E. Bykova, L. Dubrovinsky, M. Hanfland, H.-P. Liermann, and S. van Smaalen, Pressure-induced normal-incommensurate and incommensurate-commensurate phase transitions in CrOCl, Sci. Rep. **5**, 9647 (2015).

[26] H. Schäfer and F. Wartenpfuhl, Das Chrom(III)-oxychlorid CrOCl, Z. Anorg. Allg. Chem. **308**, 282 (1961).

[27] H.-E. Forsberg, On the structure of CrOCl, Acta Chem. Scand. **16**, 777 (1962).

[28] K. Nocker and R. Gruehn, Zum chemischen Transport von CrOCl und Cr_2O_3 - Experimente und Modellrechnungen zur Beteiligung von $CrOCl_{2,g}$, Z. Anorg. Allg. Chem. **619**, 699 (1993).

[29] R. Boehler and K. de Hantsetters, New anvil designs in diamond-cells, High Press. Res. **24**, 391 (2004).

[30] S. Klotz, J.-C. Chervin, P. Munsch, and G. Le Marchand, Hydrostatic limits of 11 pressure transmitting media, J. Phys. D **42**, 075413 (2009).

[31] H.-P. Liermann, Z. Konôpková, W. Morgenroth, K. Glazyrin, J. Bednarčik, E. E. McBride, S. Petitgirard, J. T. Delitz, M. Wendt, Y. Bican, A. Ehnes, I. Schwark, A. Rothkirch, M. Tischer, J. Heuer, H. Schulte-Schrepping, T. Kracht, and H. Franz, The extreme conditions beamline P02.2 and the extreme conditions science infrastructure at PETRA III, J. Synchrotron. Rad. **22**, 908 (2015).

[32] G. Shen, Y. Wang, A. Dewaele, C. Wu, D. E. Fratanduono, J. Eggert, S. Klotz, K. F. Dziubek, P. Loubeyre, O. V. Fat'yanov, P. D. Asimow, T. Mashimo, R. M. M. Wentzcovitch, and other members of the IPPS task group, Toward an international practical pressure scale: A proposal for an IPPS ruby gauge (IPPS-Ruby2020), High Press. Res. **40**, 299 (2020).

[33] F. Datchi, A. Dewaele, P. Loubeyre, R. Letoullec, Y. Le Godec, and B. Canny, Optical pressure sensors for high-pressure studies in a diamond anvil cell, High Press. Res. **27**, 447 (2007).

[34] See Supplemental Material at http://link.aps.org/supplemental/10.1103/PhysRevB.108.104108 for details about data processing and structure refinements, as well as for values of experimental and structural parameters and t-plots of interatomic distances, which includes Refs. [22,25,27,31,35,36,40–42,49–53].

[35] Rigaku Oxford Diffraction, *CrysAlis^{pro}* software system, Rigaku Corporation (2019).

[36] V. Petříček, M. Dušek, and L. Palatinus, Crystallographic computing system JANA2006: General features, Z. Krist. **229**, 345 (2014).

[37] T. Hahn, ed., *International Tables for Crystallography. Volume A: Space-group Symmetry* (Springer, Dordrecht, 2005).

[38] H. T. Stokes, B. J. Campbell, and S. van Smaalen, Generation of (3 + d)-dimensional superspace groups for describing the symmetry of modulated crystalline structures, Acta Cryst. A **67**, 45 (2011).

[39] R. K. Crawford and W. B. Daniels, Experimental determination of the P–T melting curves of Kr, Ne, and He, J. Chem. Phys. **55**, 5651 (1971).

[40] F. Birch, Finite elastic strain of cubic crystals, Phys. Rev. **71**, 809 (1947).

[41] R. J. Angel, Equations of state, Rev. Mineral. Geochem. **41**, 35 (2000).

[42] J. Gonzalez-Platas, M. Alvaro, F. Nestola, and R. Angel, EosFit7-GUI: A new graphical user interface for equation of state calculations, analyses and teaching, J. Appl. Cryst. **49**, 1377 (2016).

[43] P. Vinet, J. Ferrante, J. H. Rose, and J. R. Smith, Compressibility of solids, J. Geophys. Res.: Solid Earth **92**, 9319 (1987).

[44] M. Bykov, E. Bykova, S. van Smaalen, L. Dubrovinsky, C. McCammon, V. Prakapenka, and H.-P. Liermann, High-pressure behavior of FeOCl, Phys. Rev. B **88**, 014110 (2013).

[45] H. T. Stokes and D. M. Hatch, *Isotropy Subgroups of the 230 Crystallographic Space Groups* (World Scientific, Singapore, 1988).

[46] J. Zhang, A. Wölfel, L. Li, S. van Smaalen, H. L. Williamson, and R. K. Kremer, Magnetoelastic coupling in the incommensurate antiferromagnetic phase of FeOCl, Phys. Rev. B **86**, 134428 (2012).

[47] S. Klotz, K. Komatsu, A. Polian, S. Machida, A. Sano-Furukawa, J.-P. Itie, and T. Hattori, Crystal structure and magnetism of MnO under pressure, Phys. Rev. B **101**, 064105 (2020).

[48] A. Schönleber, J. Angelkort, S. van Smaalen, L. Palatinus, A. Senyshyn, and W. Morgenroth, Phase transition, crystal structure, and magnetic order in VOCl, Phys. Rev. B **80**, 064426 (2009).

[49] S. van Smaalen, *Incommensurate Crystallography* (Oxford University Press, Oxford, 2012).

[50] M. Bykov, Structural aspects of pressure- and temperature-induced phase transitions in low-dimensional systems, Ph.D. thesis, Universität Bayreuth, Bayreuth, Germany (2015).

[51] E. Bykova, Single-crystal x-ray diffraction at extreme conditions in mineral physics and material sciences, Ph.D. thesis, University of Bayreuth, Bayreuth (2015).

[52] K. Friese, A. Grzechnik, J. M. Posse, and V. Petříček, Refinement of high pressure single-crystal diffraction data using Jana2006, High Press. Res. **33**, 196 (2013).

[53] P. J. Becker and P. Coppens, Extinction within the limit of validity of the Darwin transfer equations. I. General formalism for primary and secondary extinction and their applications to spherical crystals, Acta Cryst. A **30**, 129 (1974).